ELSEVIER

Neurobiology of Aging 32 (2011) 894–906

NEUROBIOLOGY OF AGING

www.elsevier.com/locate/neuaging

Age-associated cerebral atrophy in mouse lemur primates

Audrey Kraska [a,b], Olene Dorieux [a,b,c], Jean-Luc Picq [c,d], Fanny Petit [a,b], Emmanuel Bourrin [a,b,e], Evelyne Chenu [f], Andreas Volk [f], Martine Perret [c], Philippe Hantraye [a,b], Nadine Mestre-Frances [g], Fabienne Aujard [c], Marc Dhenain [a,b,h,*]

[a] CEA, DSV, I2BM, MIRCen, 18 route du panorama, 92265 Fontenay-aux-Roses Cedex, France
[b] CNRS, URA CEA CNRS 2210, 18 route du panorama, 92265 Fontenay-aux-Roses Cedex, France
[c] CNRS UMR 7179, MNHN, 4 Av du Petit Château, 91800 Brunoy, France
[d] Laboratoire de psychopathologie et de neuropsychologie, E.A. 2027, Université Paris 8, 2 rue de la liberté, 93000 St Denis, France
[e] Institut de Recherche SERVIER, 125 Chemin de Ronde, 78290 Croissy-sur-Seine, France
[f] Institut Curie, U759 INSERM, Centre Universitaire, Labo 112, 91405 Orsay Cedex, France
[g] INSERM U710, EPHE, Université Montpellier 2, Place Eugène Bataillon, 34095 Montpellier Cedex 5, France
[h] CEA, DSV, I2BM, NeuroSpin, Centre CEA de Saclay, Bât. 145, 91191 Gif sur Yvette, France

Received 12 December 2008; received in revised form 3 April 2009; accepted 27 May 2009
Available online 28 June 2009

Abstract

We assessed the regional brain atrophy in mouse lemur primates from 4.7 T T2-weighted magnetic resonance images. Thirty animals aged from 1.9 to 11.3 years were imaged. Sixty-one percent of the 23 animals older than 3 years involved in the study displayed an atrophy process. Cross-sectional analysis suggests that the atrophy follows a gradual pathway, starting in the frontal region then involving the temporal and/or the parietal part of the brain and finally the occipital region. Histological evaluation of five animals selected according to various stages of atrophy suggested that extracellular amyloid deposits and tau pathology cannot explain by themselves this atrophy and that intracellular amyloid deposition is more closely linked to this pathology. This study suggests that most of the age-related atrophy occurring in mouse lemurs is caused by one clinical, evolving, pathological process. The ability to follow this pathology non-invasively by MRI will allow to further characterize it and evaluate its relationship with neuropathological lesions that are involved in human diseases such as Alzheimer.

Keywords: Alzheimer's disease; Amyloid; Animal models; Atrophy; MRI; Tau

1. Introduction

In humans, cerebral atrophy occurs in the course of aging (Dekaban and Sadowsky, 1978; Good et al., 2001) and also in many age-related neurodegenerative diseases (Valk et al., 2002). The location and rate of atrophy depends on underlying pathological processes (Tisserand et al., 2004). For example, during Alzheimer's disease (AD) the atrophy starts in temporal areas and progressively reaches all the brain regions (Baron et al., 2001). In fronto-temporal dementia, the atrophy is more prominent in the frontal lobes and anterior temporal regions (Bocti et al., 2006).

Animal models are critical to improve our understanding of age-related neurodegenerative diseases and to develop new treatments against these diseases. To date, most of the animal studies in the field of AD are based on transgenic mice (Delatour et al., 2006a; Lee et al., 2005). Although very useful, these models do not reproduce all the aspects of human pathologies. In particular their cerebral atrophy is not similar to that found in AD patients (Delatour et al., 2006b). Spontaneous models can be an alternative to transgenic animals. However, as for transgenics, the characterization of these models is a critical step prior to their use in therapeutic trials.

Mouse lemurs (*Microcebus murinus*) are small (about 12 cm, 100 g) primates with a mean life span of 5 years and

* Corresponding author at: URA CEA CNRS 2210, 18 route du panorama, 92265 Fontenay-aux-Roses Cedex, France. Tel.: +33 1 69 86 77 58; fax: +33 1 69 86 77 45.
E-mail address: marc.dhenain@cea.fr (M. Dhenain).

0197-4580/$ – see front matter © 2009 Elsevier Inc. All rights reserved.
doi:10.1016/j.neurobiolaging.2009.05.018

a maximum life span of 12 years in captivity (Perret, 1997). Their brain weighs approximately 1.7 g (Bons et al., 1998). It measures 23 mm from the tip of the olfactory bulbs to the caudal end of the medulla, and has a maximum width of 18 mm (Le Gros Clark, 1931). Previous studies have shown that some aged mouse lemurs can present with some of the lesions that characterize AD such as extracellular amyloid deposits (Bons et al., 1991) or altered tau proteins (Bons et al., 1994; Delacourte et al., 1995). They also display age-related iron accumulation in the brain (Dhenain et al., 1998) and cerebral atrophy (Dhenain et al., 1997). Such alterations remind human cerebral aging. In a pilot study, which concerned only the temporo-parietal area, we described in a series of 30 lemurs an atrophy process starting at an age between 5 and 8 years and evolving rapidly once initiated (Dhenain et al., 2000). In a more recent study in a limited series of 12 animals, we reported that this atrophy process shows regional specificity (Dhenain et al., 2003). In these two studies, cerebral atrophy was detected by measuring cerebrospinal fluid (CSF) volume, an index of atrophy. Despite these first studies, the cerebral pathologies displayed by the mouse lemurs are still poorly characterized. One important question is the heterogeneity of the alterations within the animal population: do most of the animals with atrophic and neuropathological alterations suffer from the same disease or are they presenting with many different clinical entities?

Thus, the first aim of the current study was to evaluate by MRI, whether or not the atrophy process observed was consistent in all animals and could reflect different stages of a single pathological process. This *in vivo* study was based on the automatic segmentation of MRI from mouse lemur brains and on the automated quantification of CSF volumes in various pericortical regions. As in our previous studies, CSF volumes in various regions surrounding the cortex were used as indexes of regional atrophies. Results showed focal, multi-focal and generalized atrophy patterns. These patterns were consistent with a progression of the atrophy starting from sharply demarcated regions toward a more generalized process encompassing the whole brain. In addition, neuropathological alterations were assessed in subgroups of aged lemurs selected according to different stages of localized and generalized atrophy. Intracellular and extracellular accumulations of amyloid, slight tau pathology as well as increased gliosis were found in various animals. Interestingly, the atrophied animals were those with the most severe neuropathology suggesting that aging in mouse lemurs can be associated with a progressive and consistent pattern of neurono-glial alterations and cerebral atrophy.

2. Materials and methods

2.1. Subjects

Thirty mouse lemurs aged from 1.9 to 11.3 years (young adult (from 1.9 to 2.5 years old, $n = 7$), middle-aged animals (from 3 to 5.9 years old, $n = 11$), and aged animals (6.4–11.3 years, $n = 12$), born and raised in a laboratory breeding colony at Brunoy (France, agreement no. 962773), were involved in the MRI study (Table 1). The brain of 5 of these animals, aged from 6.4 to 11.2 years, presenting with various atrophy levels (Table 2) were evaluated post-mortem. The delay between MRI and death of these animals was less than 1 year.

2.2. MRI evaluation of cerebral atrophy

2.2.1. In vivo three dimensional MR imaging

Brain images were recorded according to previously published protocols (Dhenain et al., 2003) on a 4.7 T Bruker Biospec 47/30 system by using a surface coil (diameter = 30 mm) actively decoupled from the transmitting birdcage probe (Bruker GmbH). Briefly, animals were pre-anesthetized with atropine (0.025 mg/kg subcutaneously) and anesthetized by isoflurane. Respiration rate was monitored to insure animal stability until the end of the experiment. Body temperature of the mouse lemur was maintained by using water filled heating blanket. Three-dimensional inversion-recovery fast spin-echo images (IR-RARE) were recorded with an isotropic nominal resolution of 234 μm (TR/TE = 2500/6 ms, TEw = 45 ms, TI = 200 ms, RARE-factor = 16).

2.2.2. Image post-processing and segmentation protocol

MR images were processed as described in Fig. 1: first, the sensitivity gradient resulting from surface coil acquisition was corrected by a phantom based method that we previously validated (Fig. 1A) (Dhenain et al., 2003). Briefly, images of a 2.5% agar and NaCl 0.09% phantom were recorded under the same conditions as the brain images. Time domain data were filtered by a sine-squared function to enhance signal to noise ratio. Then, the 3D matrix that yielded isointense images of the phantom was calculated and applied to brain images (code written under IDL 5.4, Research Systems Inc.).

Intensity non-uniformity in brain images was further slightly corrected before to apply the segmentation protocols. First, the brain and surrounding CSF were automatically extracted from other head tissues by using the freely available BrainVisa software (http://brainvisa.info/download.html) (VipGetBrain and VipClosing routines; Fig. 1B) (Mangin et al., 1998). The two eyes were also extracted by using the same routines. The non-uniformity in MR images intensity was corrected by using an automatic method based on the minimization of the entropy within the images also by using the BrainVisa software (Fig. 1C; VipBiasCorrection routine (Mangin, 2000)). This was performed in a three step manner: the correction was applied to the brain alone, then to the eyes, finally it was performed for the brain and the eyes that were put back together on the images (Kregul 10.0; Dimfield 3; Sampling 40.0; Grid 2.00). Then the images of the brain and of the eyes were automatically segmented by using published segmentation algorithms (Fig. 1D) (Dhenain et al., 2003). Briefly, in a preliminary step, before the segmentation proce-

Table 1
Overview of animals involved in the study. Age during MR exam, age at death and survival are in years.

Age during MR exam[a]	Atrophy stage	Ophthalmologic exam	Age at death	Survival after MRI
Young ($n = 7$)				
1.9	St. 0	Well seeing	9.3	7.4
1.9	St. 0	Well seeing	5.8	3.9
2.1	St. 0	Well seeing	2.6	0.5
2.1	St. 0	Well seeing	5.7 (sacrificed)	NA
2.2	St. 0	Well seeing	3.3 (sacrificed)	NA
2.4	St. 0	Well seeing	6.1	3.7
2.5	St. 0	Well seeing	9.9	7.4
Middle aged ($n = 11$)				
3.6	St. 0	Well seeing	7.4	3.8
3.6	St. 0	Well seeing	3.8 (sacrificed)	NA
5.0	St. 0	Well seeing	6.2	1.2
5.1	St. 0	Well seeing	8.0	2.9
5.3	St. 0	Well seeing	7.4 (sacrificed)	NA
5.5 (H1)	St. 0	Immature cataract of the left eye	6.3	0.9
3.0	St. 1	Well seeing	6.8	3.8
5.8	St. 1	Well seeing	7.6	1.8
5.9	St. 2a	Well seeing	6.1	0.2
5.8	St. 2a	Immature cataract of the right eye	7.9	2.2
3.9	St. 3	Well seeing	9.7	5.8
Aged ($n = 12$)				
6.4 (H2)	St. 0	Well seeing	7.3	0.8
6.9	St. 0	Well seeing	9.8	2.8
6.9	St. 0	Visual impairment but not blind (right eye: cataract + luxation of the lens; left eye: normal)	7.6	0.6
7.0	St. 1	Well seeing	8.5	1.4
6.9	St. 2b	Well seeing	7.1	0.2
7.6 (H3)	St. 2a	Visual impairment but not blind Incipient bilateral cataract	8.0	0.4
9.4	St. 2a	Visual impairment but not blind (right eye altered; left eye normal)	10.4	1.1
7.5	St. 4a	Well seeing	8.7	1.3
8.8 (H4)	St. 4b	Blind bilateral keratitis, thick white deposits on both corneas	8.8	0.0
11.3 (H5)	St. 4b	Blind Severe bilateral cataract	11.9	0.6
10.2	St. 4b	Blind severe bilateral cataract + calcic deposits on the cornea	11.1	0.9
10.9	St. 4b	Blind severe bilateral cataract	11.1	0.2

[a] The terms H1–5 refer to the animals that have been studied by histology (see Table 2).

Table 2
Overview of neuropathological findings in the animals studied by MRI.

Aal	Age	Atrophy	Amyloid			GFAP		CP13	
			Cx	Hip	Deposits	Cx	Hip	Cx	Hip
H1	6.3	Stage 0	+	+	No	0	0	0	+
H2	7.3	Stage 0	++	+	No	0	+	0	0
H3	8.0	Stage 2a	+	++	Yes	++	0	0	0
H4	8.8	Stage 4b	+	+++	No	0	++	0	+
H5	11.9	Stage 4b	++	+++	Yes	++	+++	0	+

The atrophy patterns are showed in the third column. The following columns correspond to intracellular amyloid deposits, extracellular deposits, CP13 and GFAP stainings in the cortex (Cx) and hippocampus (Hip), respectively. Stainings are graded as follows: (0) no labeling; (+) slight labeling; (++) moderate labeling; (+++) high labeling. The names of the animals (H1–5) refer to the Table 1. Ages at death are in years. H1 and H2 animals died at the end of the winter season after a quick loss of weight (from 110 to 70 g in one month). The other animals were older and died without apparent health issues. Autopsies did not reveal any obvious alterations in these animals.

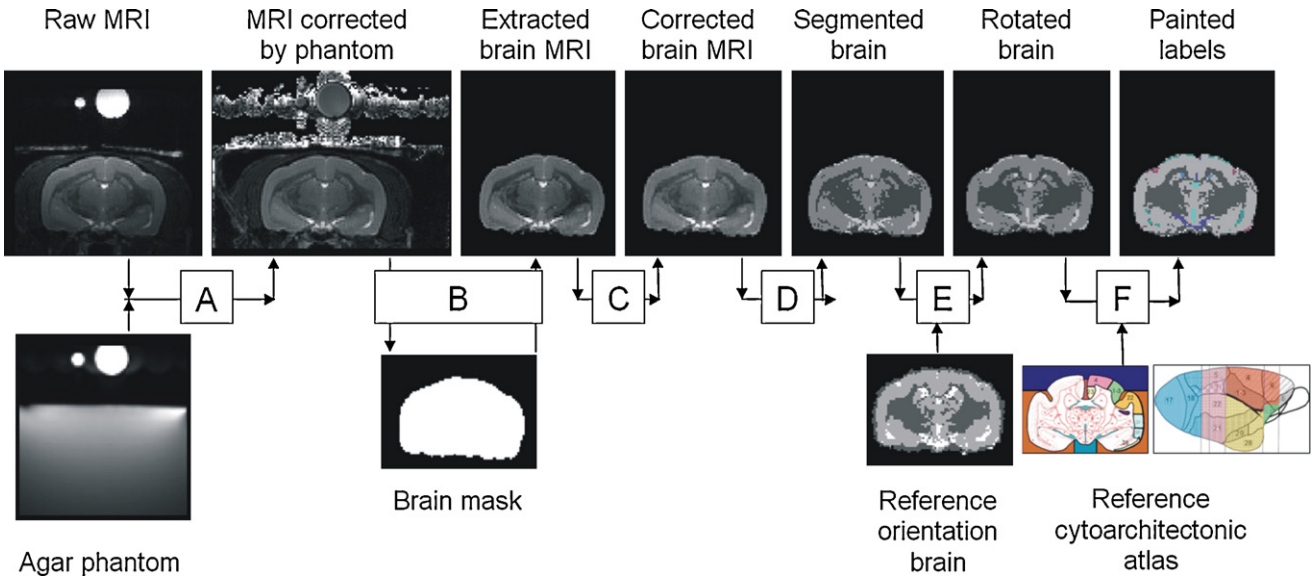

Fig. 1. Processing pipeline used in the current study. (A) Correction of sensitivity gradient resulting from surface coil acquisition by using a phantom based method (Dhenain et al., 2003). (B) Creation of a mask for the brain and brain extraction thanks to this mask. (C) Further slight correction for intensity non-uniformity in MR images. Note that this modification was minor as compared to the phantom-based correction. (D) Mahalanobis-segmentation. (E) Rotation of the 3D maps so that all the maps had the same orientation as a reference mouse lemur brain. (F) Classification of CSF pixels according to their region of origin. Attribution of the voxels to various regions was based on a reference atlas of CSF location.

dure, the bit depth of MR images was reduced from 32 to 8 and the high intensity artifactual voxels were removed (Dhenain et al., 2003). Then, the automatic statistical segmentation protocol based on a classification–maximization algorithm that we previously developed was applied to the images to detect the thresholds that separated white matter (WM), gray matter (GM), and fluid (Dhenain et al., 2003). This technique allows unsupervised partitioning of voxels into four pre-defined bins (WM, GM, fluid, and one 'background'). Briefly, the algorithm performed voxel segmentation in two steps: (1) First, for each bin it estimated the bin mean (μ), variance ($\sigma 2$), and fractional probability (πk). Then an iterative optimization of voxel attribution to the various bins was based on the calculation of modified Mahalanobis distance. (2) During the final segmentation step, each voxel in the original input volume was segregated into its final tissue bin destination using a Gaussian probability equation, with the final estimated bin parameters computed in step 1 as coefficients (see (Dhenain et al., 2003) for a more focused description of the method).

The segmented MRI maps from the different mouse lemurs were rotated and shifted so that all the maps had the same orientation (Fig. 1E; code written under IDL 5.4) (see Dhenain et al., 2003). The orientation corresponded to that of a reference mouse lemur brain that we previously used as a reference for MRI analysis (Dhenain et al., 2003).

2.2.3. Regional evaluation of CSF volumes

In the present study, we focused on the CSF voxels that were localized between the frontal lobe and the occipital part of the brain. The most frontal slice taken into account was the first slice where the olfactory bulb was not detected anymore. CSF pixels were classified (Fig. 1F) according to their region of origin by using the following nomenclature: First, the ventricles were classified into three regions: the third ventricle (3V), the lateral ventricles (LV), and the external part of the temporal horns of the lateral ventricles (ETH). CSF from all the periencephalic spaces were categorized into various regions, called RPES (regions of the periencephalic spaces) as previously described (Dhenain et al., 2003). The RPES corresponded to regions that were directly surrounding the cortex (Fig. 2). They were identified as (1) the frontal (medio-dorsal) and parietal cortex (FPcort), (2) the frontal ventral region (Fvcort), (3) the temporal cortex (Tcort), (4) the secondary parieto-temporal cortex including the CSF localized in the interhemispheric fissure in the slab where the parieto-temporal cortex was defined (PTcort), (5) the occipital cortex

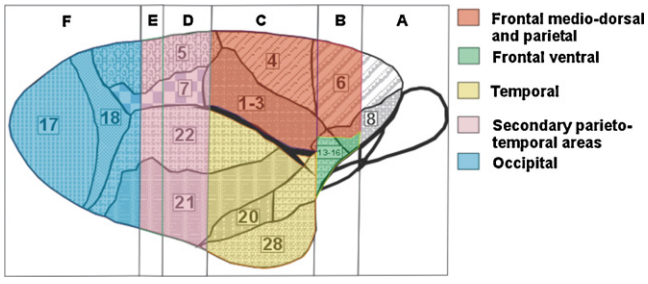

Fig. 2. Colored transparent layers corresponding to the RPES, pasted on a lateral view of the brain. Letters correspond to various slabs that were used to define brain regions (A: Anterior 1; B: Anterior 2; C: Medium 1; D: Medium 2; E: Posterior 1; F: Posterior 2; see Dhenain et al., 2003 for further description of the method). Some RPES were indeed defined on different slabs. For example the frontal medio-dorsal and parietal region was defined on the Anterior 2 and Medium 1 slabs. Numbers on the background layer refer to cytoarchitectural areas defined by Le Gros Clark (1931).

(Ocort), and (6) the interhemispheric fissure in the most anterior parts of the brain (IHfiss). The method used to define the RPES has been previously reported (Dhenain et al., 2003). Briefly, RPES definition was based on the use of reference landmarks that could be easily identified on MR images and on the cytoarchitectural atlas of the mouse lemur brain by Le Gros Clark (1931). Because it is relatively straightforward to associate a MR slice to a given section from the atlas, the first landmarks were the sections from the atlas (Le Gros Clark, 1931). They were used to divide the brain into five coronal slabs (Fig. 2). In the second step, easily visible anatomical landmarks such as sulci or fissures, shape, and curvature of the white matter and of the brain, were used to define several "preliminary" RPES (pre-RPES) within each slab. For example, the Sylvian fissure separated temporal and parietal pre-RPES in the medium 1 slab. Seventeen pre-RPES were defined to classify the CSF from all the periencephalic spaces (see Dhenain et al., 2003 for further description of the method). The criteria used to separate each slab and pre-RPES within each slab were meticulously noted and reported in an intranet web site (data not shown). Pre-RPES from different slabs were then assembled to define the final RPES.

Thanks to this method, the voxels categorized as CSF by the automatic segmentation were manually labeled and classified as belonging to one of the ventricle regions or pre-RPES (Fig. 1F). CSF painting was performed by two evaluators (MD and EC). Once all images from all the animals had been labeled, we double-checked that the voxel attribution to the different ventricle regions and pre-RPES was consistent across animals and between the two evaluators. Then, the number of voxels belonging to each region was automatically counted ('Display' freeware (http://www.bic.mni.mcgill.ca/software/Display/Display.html)). A total brain atrophy index was also calculated by summing up CSF volumes from all the RPES and ventricles and a total cortical atrophy index was computed by adding CSF volumes from all regions surrounding the cortex. Intraclass correlation coefficients were calculated to evaluate the measures performed by the two evaluators before and after the control of the consistency of CSF labeling. The obtained coefficients ranged from 0.98 to 1 for the nine evaluated RPES and was equal to 0.97 and 1 for the total cortical atrophy and total atrophy indexes, respectively.

2.2.4. Staging of the atrophy in individual animals

For individual studies, regional atrophy from cortical areas (FPcort, Fvcort, Tcort, PTcort and Ocort) was quantified for each animal with a three grade scale (0: no atrophy; +: moderate atrophy; ++: severe atrophy). To define the thresholds between the atrophy grades, animals younger than 3 years were taken as reference. The thresholds were Mcsf + ($C \times$ SDcsf) where Mcsf and SDcsf were the mean and standard deviation for CSF estimate in a given brain area for young adults. C was a constant equal to 2.58 (1% confidence interval of a Gaussian population) for the threshold between 0 and + levels, and 5 (arbitrary value) for the threshold between+ and ++ levels. The atrophy was then represented on brain maps that showed the spatial location of the atrophy with a color code (0: blue; +: pink; ++: red).

2.3. Neuropathology

2.3.1. Tissue processing and histochemical staining

The mouse lemur brains were removed and fixed in 4% formalin after the natural death of animals. The brains were split into their right and left hemispheres. The right hemisphere from each animal was sectioned on the coronal plane on a cryostat (40-μm-thick sections) whereas the left hemisphere was used for paraffin sectioning (6-μm-thick sections) and sectioned following a sagittal plane. Right hemispheres were plunged 24 h in a 15% and then 30% sucrose solution for cryoprotection. They were then frozen and sliced into 40-μm-thick coronal sections on a freezing Microtome. Slices were then stored at −20 °C into a storage solution (Glycerol 30%, ethylene glycol 30%, and phosphate buffer 0.1 M). Then, floating sections were rinsed with 0.1 M phosphate buffer and mounted on Superfrost plus glass slides before being stained for amyloid-β and Glial Fibrillary Acidic Protein (GFAP) detection. For anti-Aβ (biotinylated mouse monoclonal 4G8 antibody, Biovalley) and anti-GFAP (Rabbit Anti-GFAP, DAKO) immunohistochemistry, the brain samples were pretreated with hydrogen peroxide (0.3%). Then they were bathed into a Phosphate Buffer's (0.1 M) Saline's (0.9%) and Triton's (Sigma 100×, 0.2%) solution (PBS + Tx) with Normal Goat Serum (NGS) (Sigma G6767, 4.5%). Then, during two days, the samples were incubated into a solution of PBS + Tx with NGS (3%) and the primary antibody (concentrations of 1/1000 and 1/5000 for anti-amyloid and anti-GFAP, respectively). Then the samples were bathed for one hour into a solution PBS + Tx with NGS (3%) with the 1/250 biotinylated anti-mouse and anti-rabbit secondary antibodies (VECTOR BA-92000 and BA-1000 respectively). Next, for amyloid staining, the signal was amplified by using avidine–biotine–vectastain complex standard (ELITE PK 6100 0.225%). For anti-GFAP staining, the antibody was first bathed in a Tyramine Biotin Reagent bath (Blast PC 2815-0897 1:1000) before being amplified by avidine–biotine–vectastain complex (0.1125%). Final reaction made use of diaminobenzidine (DAB) nickel (VECTOR, SK-4100) or DAB for two minutes as chromogen (gray–black or brown stains, respectively). Negative controls were performed by omitting the primary antibody in the procedure. Positive controls for Abeta immunochemistry were performed using formalin-fixed samples taken from the superior temporal gyrus of human Alzheimer samples received in 1994 in the R. Escourolle Laboratory of La Salpêtrière Hospital (Paris, France). Aβ studies were also performed using automated immunostaining protocols based on Ventana Discovery XT technologies. To this aim, 40-μm-thick coronal sections, mounted on Polysine glass slides, were pretreated by an automated heat induced epitope retrieval procedure

(Tris/borate/EDTA buffer, pH 8.0, 8 min at 95 °C followed by 4 min at 100 °C) and were incubated with primary antibody (biotinylated mouse monoclonal antibody 4G8, 1/250, Sigma) during 60 min. A 32 min incubation with secondary antibody (biotinylated anti-mouse antibody, 1/2000, VECTOR BA-92000) was performed before the disclosure using the ABC method with DAB as the chromogen (brown stain). Finally, the sections were counterstained with hematoxylin (Ventana Medical Systems, 760-2021) and a bluing reagent (Ventana Medical Systems, 760-2037).

The left hemisphere was embedded in paraplast and cut into 6-μm-thick serial sagittal sections. The sections were tested for the presence of tau pathology using the CP13 antibody specific for phosphorylated serine 202 (generous gift of P. Davies) (Andorfer et al., 2003). Sections were dewaxed in toluene and a graded series of alcohol solutions and were incubated with formic acid (80%) for 15 min. They were then incubated with 10% goat serum in Tris-buffered saline for 30 min and then with CP13 antibodies (1/200) during 4 days at 4 °C. Immunological complexes were detected by sequential application of a 1/100 dilution of biotinylated immunoglobulin and horseradish peroxidase labeled avidine (Vector), for 30 min each. Immunoreactivity was detected with 0.005% DAB (Sigma). Standard immunohistochemical controls were performed, including (1) omission of the primary antibody, (2) use of irrelevant secondary antibodies, and (3) use of preimmune serum. No labeling was observed for any of the various controls. As all the controls were negative, the immunoreactivity observed was considered to be specific for the antibody used.

The severity of intracellular amyloid, extracellular amyloid, tau, and GFAP loads were quantified in the cortex and ventral hippocampus, using the following semi-quantitative scale: (0) no staining; (+) slight staining; (++) moderate staining; (+++) strong staining (Fig. 3). This evaluation was performed by two researchers who were blind to the age and atrophy levels of animals. Intraclass correlation coefficients for the various measures were equal to 0.66 and 0.71 for the intracellular cortical and hippocampal amyloid, 0.91 and 0.81 for the cortical and hippocampal GFAP, and 1 for the CP13 staining.

3. Results

3.1. Regional location of the atrophy process

Fig. 4 displays typical MR images from one non-atrophied and one atrophied mouse lemur brains (5.5 and 8.8 years old, respectively, see Table 1). Maps of CSF accumulations in regions surrounding cortical regions were calculated on the basis of these images. These maps revealed different patterns of atrophy in the animals involved in this study (Fig. 5). First, some animals did not show CSF increase in any of the cortical regions. This was the case for 100%, 54% and 25% of the young, middle-aged, and old animals, respectively. These animals were classified as stage 0 animals. In all other animals there was some degree of atrophy, which followed a typical sequential pattern that permitted the partitioning of these animals into four different stages of atrophy. Stage 1 animals ($n = 3$) displayed a focal atrophy that involved only the frontal medio-dorsal and parietal (FPcort) cortical regions. Stage 2 animals ($n = 5$) had an atrophy process that in addition to the FPcort, led to CSF accumulation in another cortical region adjacent to the FPcort. For four of these animals, the additional region was the parieto-temporal cortex (PTcort) (stage 2a). It was the temporal cortex (Tcort) for one animal (stage 2b). In stage 3 animals ($n = 1$) the atrophy process involved FPcort, PTcort, and Tcort regions. Finally, in stage 4 animals ($n = 5$), CSF increases were found all around the cortical regions evaluated, i.e. FPcort, PTcort, Tcort, and occipital cortex (Ocort) ($n = 5$, stages 4a and 4b). One of these animals also displayed an increased CSF level around the frontal ventral (Fvcort) cortical region. Notably, four out of these five "stage 4" animals were blind. Three of these animals had bilateral mature cataract; one also had a severe bilateral keratitis whereas the last one had a severe bilateral keratitis leading to an opaque deposit on the whole cornea,

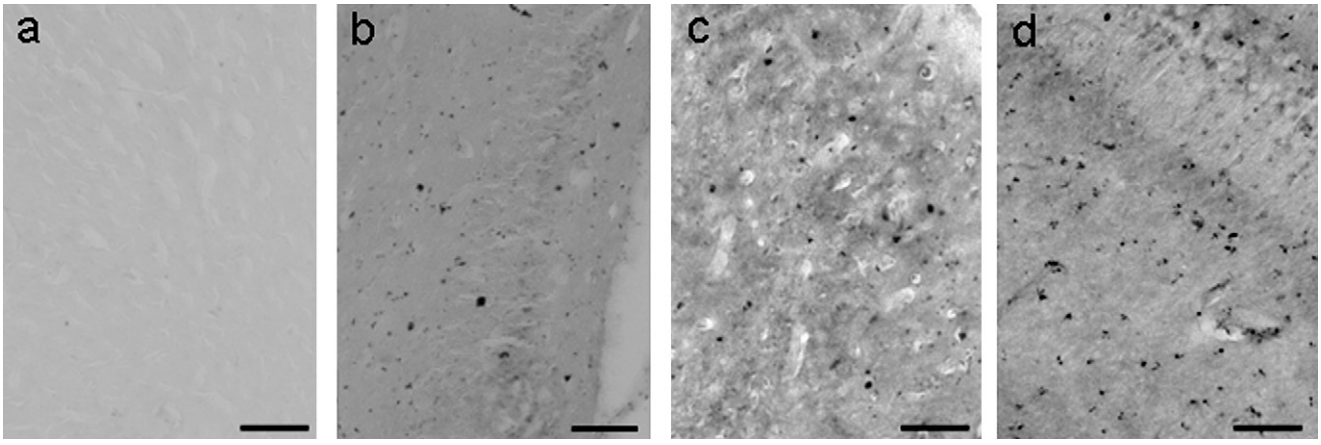

Fig. 3. Anti-amyloid labeling (4G8) in the hippocampus (a–b–c–d) of mouse lemurs aged of 8.8, 6.4, 8.0, and 11.2 years, respectively. No staining (a), slight staining (b), moderate staining (c) and strong staining (d). Scale bars represent 100 μm.

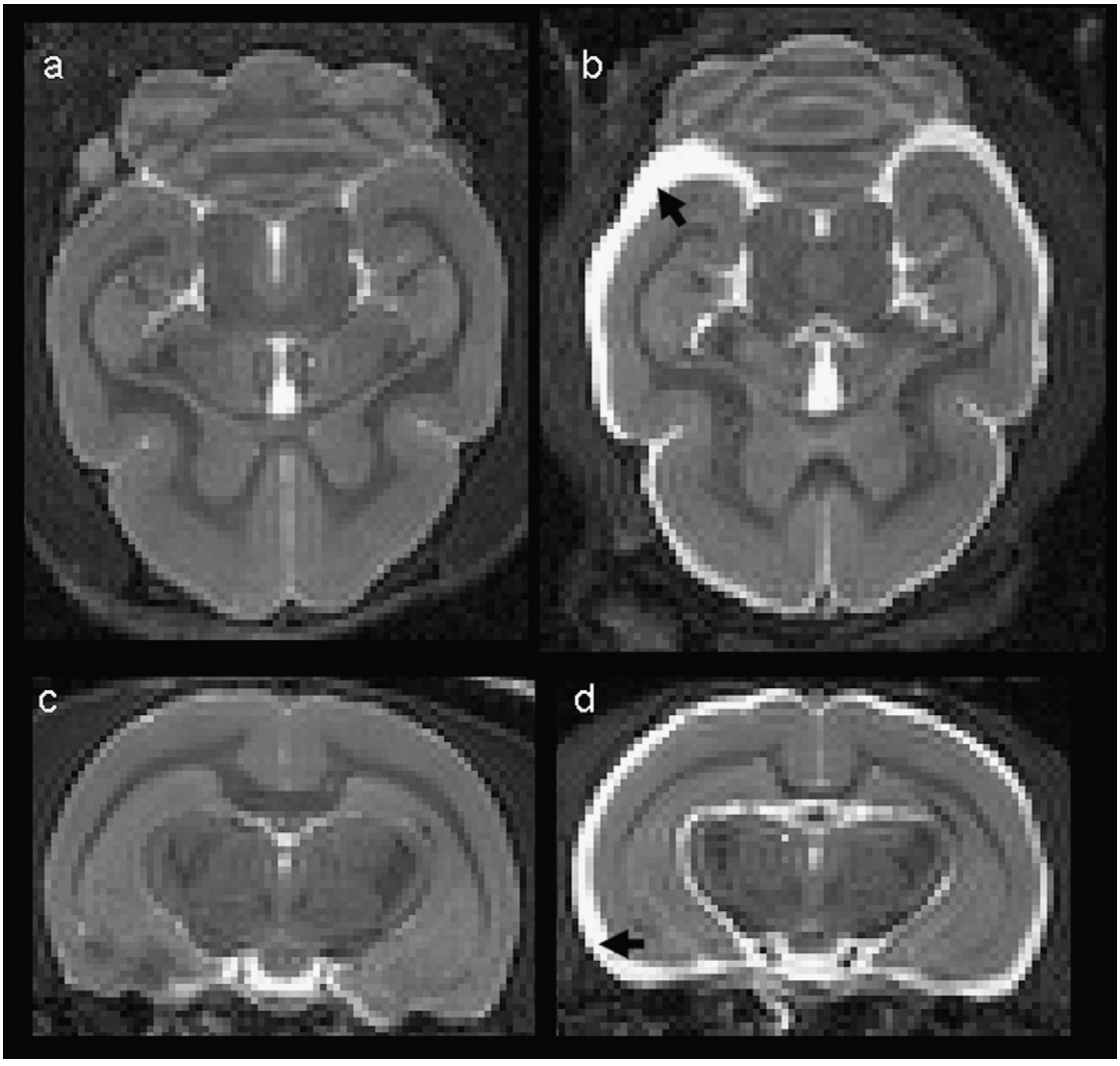

Fig. 4. Horizontal (a and b) and coronal (c and d) images from a 5.5 years non-atrophied animal as compared to a 8.8 years atrophied animal. White CSF surrounding cortical regions is obvious in the atrophied animal (arrow).

Stages	Stage 0	Stage 1	Stage 2a	Stage 2b	Stage 3	Stage 4a	Stage 4b
Atrophy Grades ++ + 0		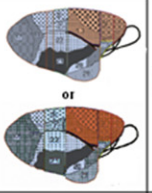		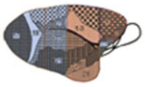	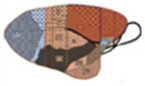	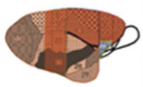	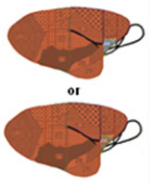
Young	7	0	0	0	0	0	0
Middle aged	6	2	2	0	1	0	0
Aged	3	1	2	1	0	1	4

Fig. 5. The maps of CSF accumulation in regions surrounding cortical regions revealed several stages of cerebral atrophy in the studied population of animals. The number of animals displaying each stage is showed underneath the maps. Red regions correspond to very high level of CSF (CSF volumes superior to the mean + 5 × SD of the CSF volumes in young adults). Pink regions correspond to high level of CSF (CSF volumes superior to the mean + 2.58 × SD of the CSF volumes in young adults). Blue regions correspond to low CSF levels (CSF volume inferior to the mean + 2.58 × SD of the CSF volumes in young adults). Evolving patterns of CSF accumulation occurred in mouse lemurs. It started in the frontal regions and then spread rostro-caudally towards the occipital cortex.

its lens being no longer visible under slit lamp examination (data not shown). None of the other animals involved in the study, including one stage 4 animal, displayed detectable ophthalmologic alterations leading to blindness (ophthalmologic examination performed by a trained veterinarian by using an ophthalmoscope and a slit lamp after instillation of atropine in the eye (data not shown, but see Beltran et al., 2007).

General linear model was used to evaluate variables explaining survival rate in non-blind mouse lemurs (which died of natural death). Age at MRI was associated with survival rate in mouse lemurs ($F(1, 16) = 7.74$, $p < 0.05$). However, the atrophy stage was not associated to the survival rate ($F(4, 16) = 0.62$, $p > 0.05$). This suggests that atrophy did not induce an increased mortality in lemurs.

3.2. Correlative studies between age and CSF levels

Correlative studies between age and CSF volumes in various brain regions were performed in a second step of the study. The four stage 4 blind animals with a high atrophy level (Fig. 6a) were excluded from these correlative analyses as their CSF volumes were greater than those of the other animals. First we looked at global atrophy indexes. Significant correlations were found between the age of the animals and the total brain atrophy index (CSF volumes from all the RPES and ventricles; $r = 0.49$, Benjamini–Hochberg false discovery rate-adjusted p-value (BH-FDRp) < 0.05 (Benjamini and Hochberg, 1995)) (Fig. 6a) or the total cortical atrophy index ($r = 0.44$, BH-FDRp < 0.05). By looking at

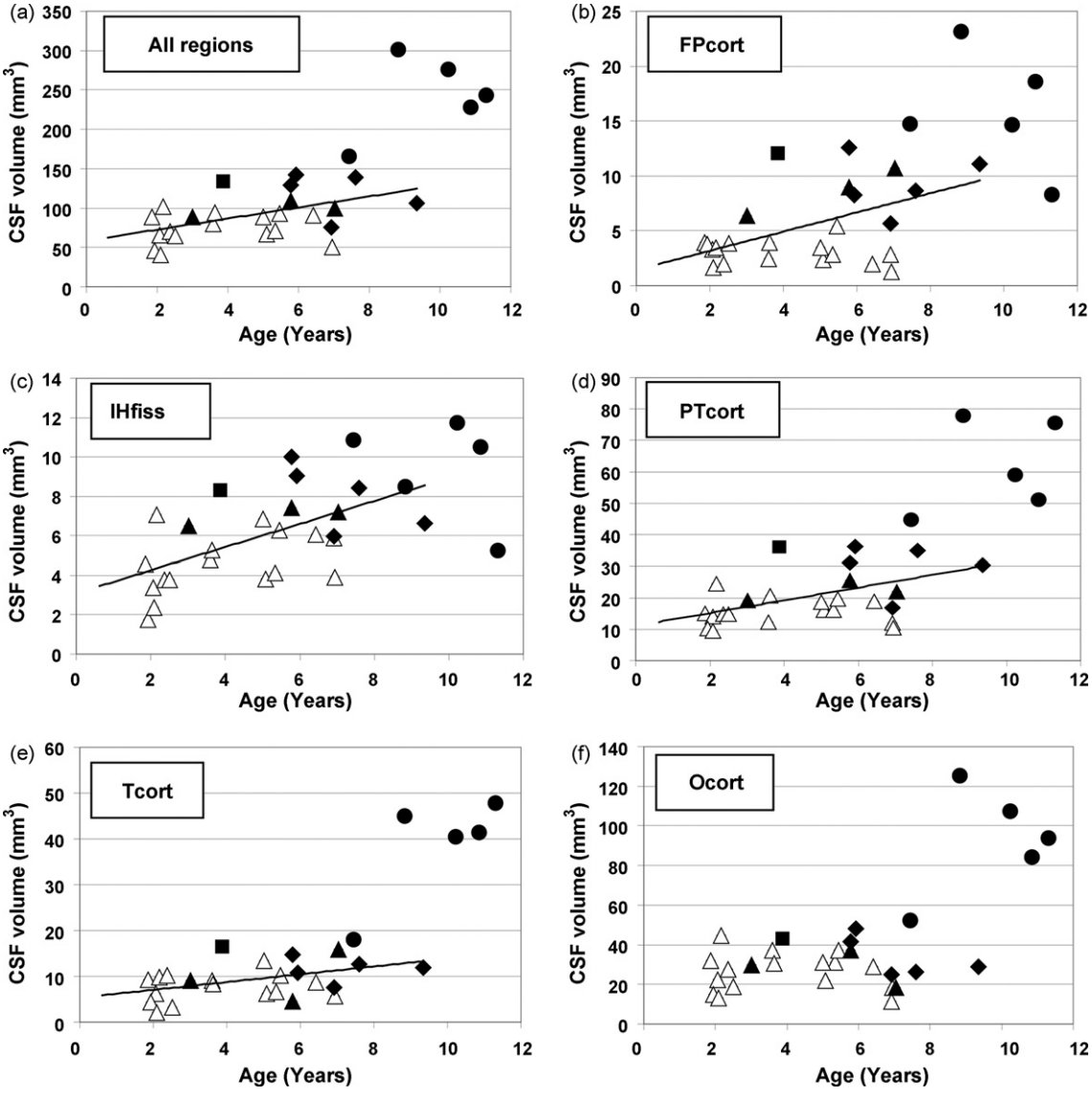

Fig. 6. CSF volumes in brain regions from the mouse lemurs involved in this study. The volume of CSF surrounding all the regions of the periencephalic spaces and ventricles (a), frontal (medio-dorsal) and parietal cortices (b), the interhemispheric fissure (c), the parieto-temporal cortex (c), the temporal cortex (d), but not the occipital cortex (f) were correlated to the age of the animals (the older animals that were blind and severely atrophied were not included in the correlative studies). Animals without regional atrophy are labeled as hollow triangles. Other animals are represented as follows. Black triangles: stage 1 atrophy pattern; black lozenges: stage 2 atrophy pattern; black squares: stage 3 atrophy pattern; black circles: stage 4 atrophy patterns.

the various regions of interest, we found a significant correlation between the age of the animals and the CSF volumes in the FPcort ($r = 0.49$; BH-FDRp < 0.05) (Fig. 6b), IHfiss ($r = 0.55$, BH-FDRp < 0.05) (Fig. 6c), PTcort ($r = 0.47$, BH-FDRp < 0.05) (Fig. 6d), Tcort ($r = 0.44$, BH-FDRp < 0.05) (Fig. 6e), third ventricle (3V) ($r = 0.49$, BH-FDRp < 0.05), and external part of the temporal horns of the lateral ventricles (ETH) ($r = 0.47$, BH-FDRp < 0.05) but not within

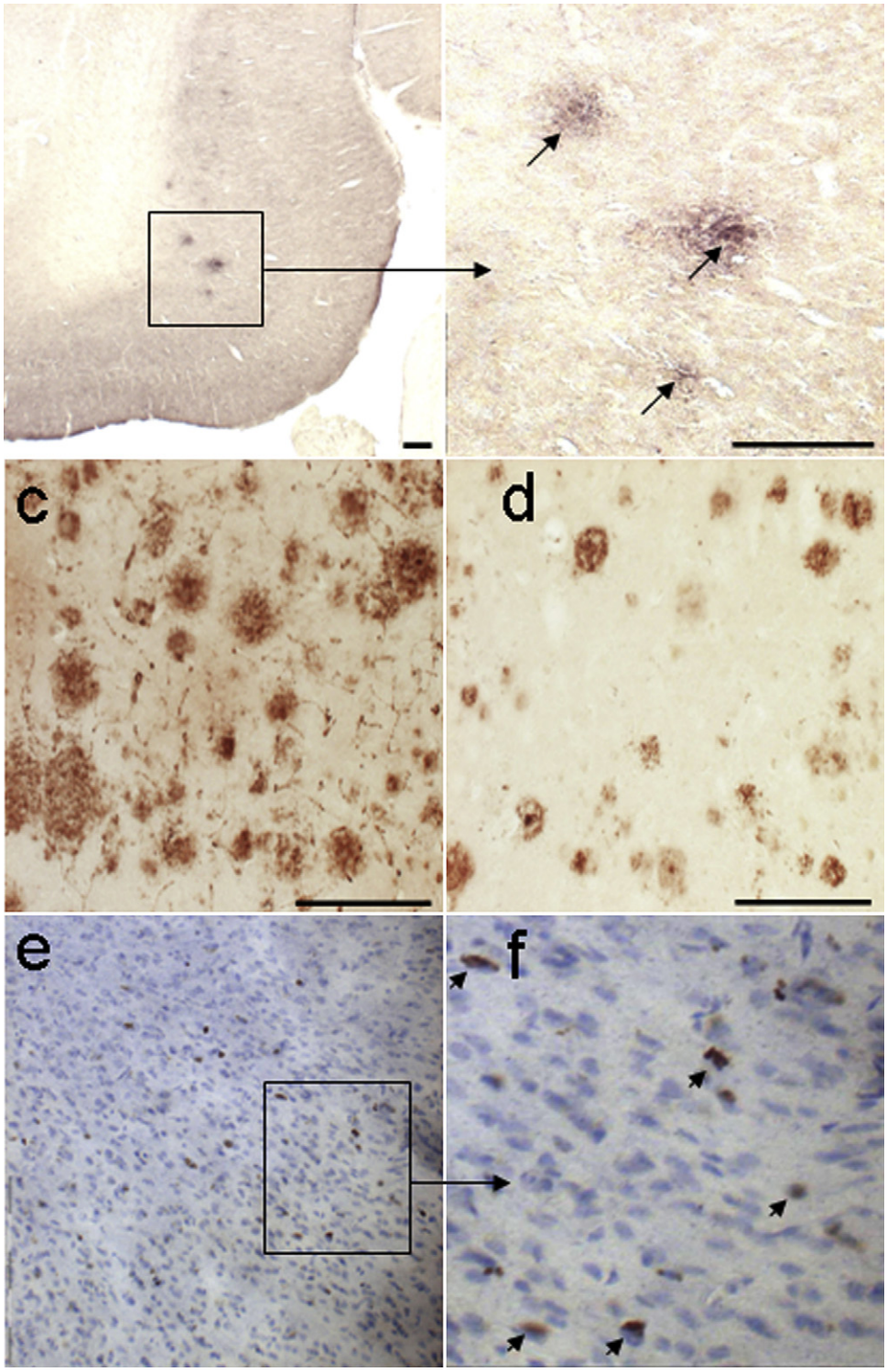

Fig. 7. Amyloid pathology in mouse lemurs. Extracellular amyloid deposits in mouse lemur at low magnification (a) and higher magnification (b, arrows). (c and d) Amyloid deposits stained with the same conditions in humans, and transgenic mouse model of AD, respectively (4G8 antibody, manual staining method). (e and f) Intracellular amyloid deposits (arrows) in the cortex of a 8.8 years old mouse lemur with a very strong intracellular amyloidosis (4G8 antibody, Ventana staining method). (a–d) Scale bars represent 200 μm.

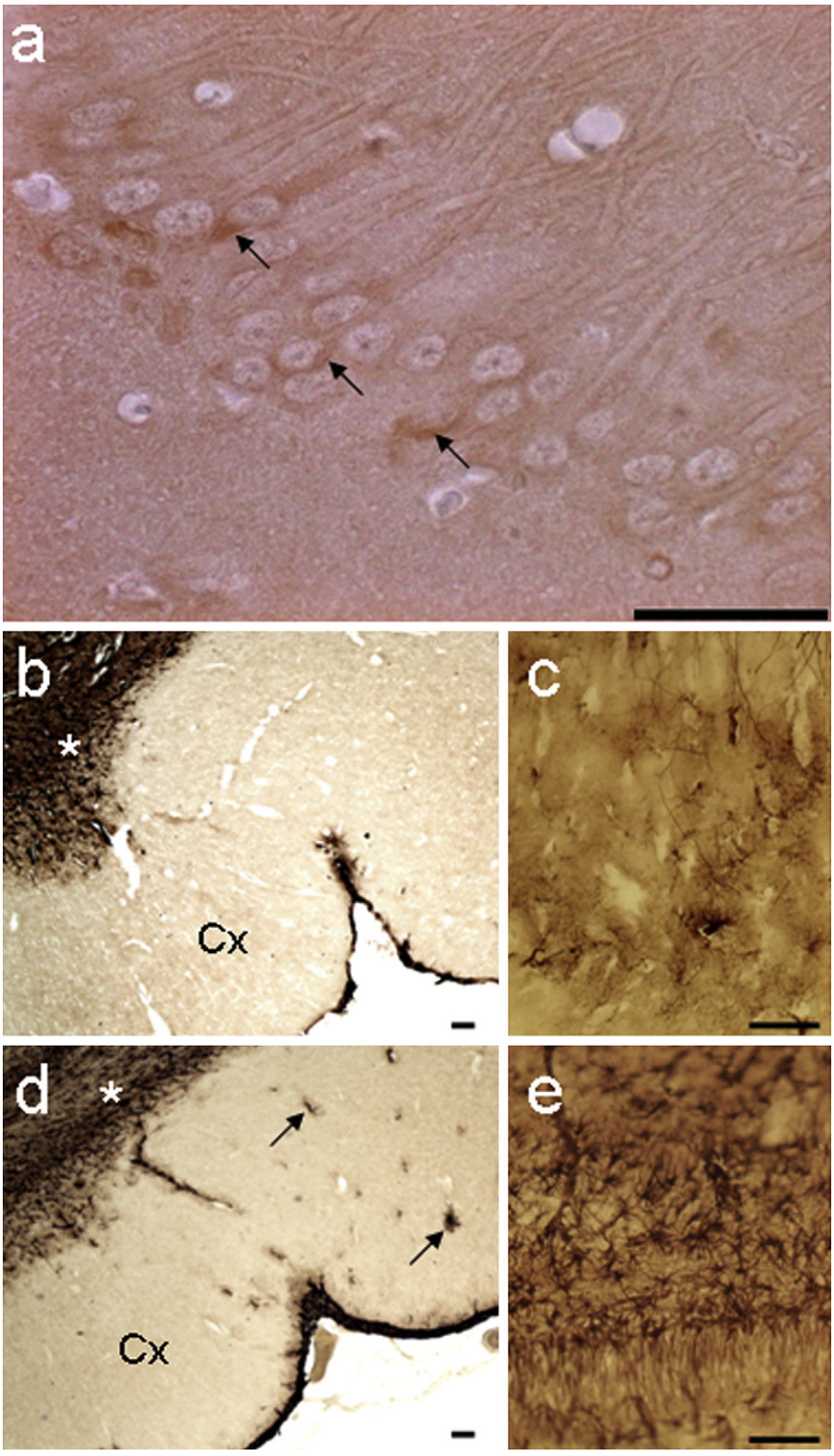

Fig. 8. (a) CP13 positive neurons (arrows) in an aged mouse lemur primate. (b–e) Anti-GFAP staining in stage 0 (b and c) and 4b (d and e) animals. The corpus callosum (asterisk) was strongly stained in all the studied animals (b and d). Cortical staining (arrow) was not detected in non-atrophied animals (b), but could be detected in atrophied ones (d). Hippocampal staining was also more obvious in the atrophied animal (e) as compared to the non-atrophied (c). Scale bars: 50 μm for CP13 (a) and 100 μm for GFAP staining (b–e).

the Fvcort, the Ocort (Fig. 6f), or the lateral ventricles (LV) (BH-FDRps > 0.05).

3.3. Neuropathological studies

Two stage 0, one stage 2 and two animals with stage 4 atrophy were included in a detailed neuropathological analysis. An overview of the histological results is presented in the Table 2.

Extracellular amyloid deposits were detected in the brain of two out of the three atrophied animals (Fig. 7a and b). In all five animals, whatever the atrophy level considered, intracellular amyloid deposition was observed in cortical and hippocampal regions either with manual (Fig. 3) or automatic staining methods (Fig. 7e and f). In the hippocampus, the intracellular amyloid load matched with the severity of atrophy (stage 0 animals had slight amyloid levels; stage 2 animals had moderate amyloid levels; stage 4 animals had high amyloid levels (Table 2)).

CP13 positive neurons were detected in the hippocampus of three animals (Fig. 8a) with CP13 staining graded + in the hippocampus of the two most severely atrophied animals (Table 2) and graded + in one stage 0 animal. No CP13 staining could be detected in the cortex of any of the animals evaluated.

GFAP immunocytochemical detection revealed a strong staining of white matter fibers such as the corpus callosum in all studied animals (Fig. 8b and d). In addition to white matter tracks, an increased GFAP staining was also observed in cortical areas (Fig. 8d) and hippocampus (Fig. 8e, Table 2), in some animals. The hippocampal labeling was more obvious in the animals displaying the highest atrophy (Table 2).

4. Discussion

In this study, we evaluated cerebral atrophy in a cohort of 30 mouse lemur primates aged from 1.9 to 11.3 years. Atrophy was quantified by estimating CSF volumes in regions surrounding the cortex. CSF pixels were determined by using an user-independent segmentation protocol that allowed to perform 3D segmented brain maps thanks to a Mahalanobis algorithm. In a previous study, we showed that results of the segmentation protocol applied to mouse lemurs are accurate and reproducible (Dhenain et al., 2003). The segmented maps of mouse lemur brains were then used to evaluate regional atrophy. In a preliminary step, all brain regions in which CSF was expected to be present were defined on reference atlases. Then the CSF voxels from the 3D segmented maps of the various animals were manually assigned to one of the defined areas by using morphological knowledge and reference atlases. Using these assays further increased the accuracy of the segmentation procedure. Thanks to this method, evaluations of CSF volumes by various evaluators led to high intraclass correlation coefficients (from 0.97 to 1).

Evaluation of ventricular and periencephalic CSF increase in various animals indicated that some animals did not show any atrophy whereas atrophy, when present, followed a typical pattern: starting in the frontal cortex region, then involving the temporal and/or the parietal part of the brain and finally the occipital region. Such patterns of atrophy were found in 14 out of the 23 middle-aged and aged animals involved in the study (i.e. 61% of these animals). When studying the full cohort of 30 animals, a significant correlation between CSF levels and age was found in many cerebral regions. However, several middle-aged and aged animals were not atrophied. This indicates that aging by itself cannot predict atrophy in mouse lemurs and that the typical pattern of cerebral atrophy observed in some middle-aged and aged animals is part of a pathological process.

In a previous study that focused on temporal regions, we showed that cerebral atrophy can occur spontaneously with aging in mouse lemurs. We showed that the age of the beginning of the atrophy can vary in various animals and that once initiated, the atrophy process can evolve rapidly (Dhenain et al., 2000). However from that study, we could not identified whether the cerebral atrophy observed corresponded to various patterns or rather to one, typical pattern of evolution. The current study allowed us to identify a gradual pathway of atrophy suggesting that one pathological entity is responsible for most of the cerebral atrophy observed in mouse lemurs. This pathology leads to CSF accumulation first in the frontal region then in the temporal and/or parietal parts of the brain and finally the occipital region.

It is notable that we focused only on evaluation of CSF volumes. As in mouse lemurs the relationship between CSF volumes and regional gray or white matter atrophy has never been studied so far, future studies will be necessary to isolate the atrophied structures at the origin of the CSF increase in pericortical regions and notably to evaluate if the CSF increase is due to cortical atrophy or rather to an atrophy of subcortical structures or white matter.

Cerebral atrophy has been largely described in human cerebral pathologies or aging. Its detection in animal models of aging and/or of AD is more controversial. Age-related, MRI-detectable, severe atrophy has been rarely described in transgenic mouse models of AD and when reported is often associated with regions that are not involved in amyloid pathology such as white matter tracts (Delatour et al., 2006a). Because of its severe age-related atrophy, the mouse lemur primate is an interesting model to evaluate age-associated cerebral atrophy.

At completion of the *in vivo* MR imaging study, we evaluated neuropathological alterations in five aged animals with stage 0, 2 and 4 atrophies. As it is often the case with mouse lemurs, the studied animals died quickly without obvious pathology (two animals lost a lot of weight during their last month of life). Tau pathology which was detected in two severely atrophied animals but also in one non-atrophied mouse lemur cannot explain the cerebral atrophy. Diffuse extracellular amyloid deposits were also detected in two of

the atrophied animals. However, this amyloid extracellular deposition was low (even in one stage 4 animal) as compared to what occurs in the brain of AD patients and/or transgenic mouse models of AD. Because of the lack/weakness of amyloid plaques detection in atrophied animals, our data suggest that the cerebral atrophy is not directly caused by extracellular amyloid deposition. On the other hand, our present data suggest a relationship between atrophy and intracellular amyloid deposition. Indeed, all the atrophied animals had high intracellular accumulation of β amyloid in the hippocampus. Intracellular Aβ deposition preceding extracellular deposition (Wirths et al., 2004) has been demonstrated in human AD (D'Andrea et al., 2001; Gouras et al., 2000), as well as in transgenic mouse models of AD (Casas et al., 2004; Oakley et al., 2006; Oddo et al., 2003; Wirths et al., 2001). This intracellular Aβ accumulation can lead to neuronal dysfunction, tau pathology, gliosis (Casas et al., 2004), apoptosis, and to cerebral atrophy (Christensen et al., 2008; Chui et al., 2001; Fernandez-Vizarra et al., 2004; Oakley et al., 2006; Wirths et al., 2004). Notably a recent study in a newly developed model of AD (APP_{T714I} mouse model), characterized by intracellular accumulation of Aβ without extracellular Aβ deposits, has shown that intracellular amyloid deposition can lead to a MRI-detectable brain atrophy even in the absence of extracellular amyloid deposition (Van Broeck et al., 2008). To our knowledge, our study is the first description of a possible link between intracellular amyloid accumulation and cerebral atrophy, in non-transgenic animals that do not overexpress mutated forms of amyloid. Future studies on a larger number of mouse lemur primates will be necessary to further characterize the pathological alterations responsible for the atrophic process described here.

In conclusion, our data suggest that cerebral atrophy in mouse lemurs is mainly related to an evolving clinical entity that occurs approximately in 60% of middle aged or aged lemurs. The pathology leads to CSF accumulation in frontal, then temporal and/or parietal part of the brain before involving in the last stage, the occipital part of the brain. Preliminary data also suggests that this pathology is associated to intracellular amyloid deposition and reactive astrocytosis. The ability to detect *in vivo* by MRI the animals with pathological aging will open new perspectives for this model of normal cerebral aging either to select homogeneous populations in clinical studies or to follow-up the effect of drug treatments against pathological aging (Bons et al., 2006; Trouche et al., 2008).

Disclosure statement

None.

Acknowledgements

We thank S. Chahory, DVM, for ophthalmologic examination of the animals involved in this study. We thank P. Davies (Albert Einstein College of Medicine, Bronx, New York) for the generous gift of the CP13 antibodies. J.F. Mangin, J. Grenèche and H. Moreira are thanked for their help during image analysis. We are grateful to E. Kremer for carefully reading and correcting the manuscript. This work was supported by the Aging ATC 2002 (INSERM), the Fédération pour la Recherche sur le Cerveau 2003, the ACI Neurosciences 2004 (French Research Department), the France-Alzheimer Association, and the National Institute on Aging (R01-AG020197).

References

Andorfer, C., Kress, Y., Espinoza, M., de Silva, R., Tucker, K.L., Barde, Y.A., Duff, K., Davies, P., 2003. Hyperphosphorylation and aggregation of tau in mice expressing normal human tau isoforms. J. Neurochem. 86 (3), 582–590.

Baron, J.C., Chetelat, G., Desgranges, B., Perchey, G., Landeau, B., de la Sayette, V., Eustache, F., 2001. In vivo mapping of gray matter loss with voxel-based morphometry in mild Alzheimer's disease. Neuroimage 14 (2), 298–309.

Beltran, W.A., Vanore, M., Ollivet, F., Nemoz-Bertholet, F., Aujard, F., Clerc, B., Chahory, S., 2007. Ocular findings in two colonies of gray mouse lemurs (*Microcebus murinus*). Vet. Ophthalmol. 10 (1), 43–49.

Benjamini, Y., Hochberg, Y., 1995. Controlling the false discovery rate: a practical and powerful approach to multiple testing. J. R. Stat. Soc. Ser. B: Stat. Methodol. 57 (1), 289–300.

Bocti, C., Rockel, C., Roy, P., Gao, F., Black, S.E., 2006. Topographical patterns of lobar atrophy in frontotemporal dementia and Alzheimer's disease. Dement. Geriatr. Cogn. Disord. 21 (5–6), 364–372.

Bons, N., Mestre, N., Petter, A., 1991. Senile plaques and neurofibrillary changes in the brain of an aged lemurian primate, *Microcebus murinus*. Neurobiol. Aging 13, 99–105.

Bons, N., Mestre, N., Ritchie, K., Petter, A., Podlisny, M., Selkoe, D., 1994. Identification of amyloid beta protein in the brain of the small, short-lived lemurian primate *Microcebus murinus*. Neurobiol. Aging 15 (2), 215–220.

Bons, N., Rieger, F., Prudhomme, D., Fisher, A., Krause, K.H., 2006. *Microcebus murinus*: a useful primate model for human cerebral aging and Alzheimer's disease? Genes Brain Behav. 5 (2), 120–130.

Bons, N., Sihol, S., Barbier, V., Mestre-Frances, N., Albe-Fessard, D., 1998. A stereotaxic atlas of the grey lesser mouse lemur brain (*Microcebus murinus*). Brain Res. Bull. 46 (1–2), 1–173.

Casas, C., Sergeant, N., Itier, J.M., Blanchard, V., Wirths, O., van der Kolk, N., Vingtdeux, V., van de Steeg, E., Ret, G., Canton, T., Drobecq, H., Clark, A., Bonici, B., Delacourte, A., Benavides, J., Schmitz, C., Tremp, G., Bayer, T.A., Benoit, P., Pradier, L., 2004. Massive CA1/2 neuronal loss with intraneuronal and N-terminal truncated Abeta42 accumulation in a novel Alzheimer transgenic model. Am. J. Pathol. 165 (4), 1289–1300.

Christensen, D.Z., Kraus, S.L., Flohr, A., Cotel, M.C., Wirths, O., Bayer, T.A., 2008. Transient intraneuronal A beta rather than extracellular plaque pathology correlates with neuron loss in the frontal cortex of APP/PS1KI mice. Acta Neuropathol. 116 (6), 647–655.

Chui, D.H., Dobo, E., Makifuchi, T., Akiyama, H., Kawakatsu, S., Petit, A., Checler, F., Araki, W., Takahashi, K., Tabira, T., 2001. Apoptotic neurons in Alzheimer's disease frequently show intracellular Abeta42 labeling. J. Alzheimers Dis. 3 (2), 231–239.

D'Andrea, M.R., Nagele, R.G., Wang, H.Y., Peterson, P.A., Lee, D.H., 2001. Evidence that neurones accumulating amyloid can undergo lysis to form amyloid plaques in Alzheimer's disease. Histopathology 38 (2), 120–134.

Dekaban, A.S., Sadowsky, D., 1978. Changes in brain weights during the span of human life: relation of brain weights to body heights and body weights. Ann. Neurol. 4, 345–356.

Delacourte, A., Sautière, P.-E., Wattez, A., Mourton-Gilles, C., Petter, A., Bons, N., 1995. Biochemical characterisation of tau proteins during cerebral aging of the lemurian primate *Microcebus murinus*. C. R. Acad. Sci. III 318, 85–89.

Delatour, B., Guegan, M., Volk, A., Dhenain, M., 2006a. In vivo MRI and histological evaluation of brain atrophy in APP/PS1 transgenic mice. Neurobiol. Aging 27 (6), 835–847.

Delatour, B., Le Cudennec, C., El Tannir-El Tayara, N., Dhenain, M., 2006b. Transgenic models of Alzheimer's pathology: success and caveat. In: Welsh, E.M. (Ed.), Topics in Alzheimer's Disease. Nova Publishers, pp. 1–34.

Dhenain, M., Chenu, E., Hisley, C.K., Aujard, F., Volk, A., 2003. Regional atrophy in the brain of lissencephalic mouse lemur primates: measurement by automatic histogram-based segmentation of MR images. Magn. Reson. Med. 50, 984–992.

Dhenain, M., Duyckaerts, C., Michot, J.-L., Volk, A., Picq, J.-L., Boller, F., 1998. Cerebral T2-weighted signal decrease during aging in the mouse lemur primate reflects iron accumulation. Neurobiol. Aging 19 (1), 65–69.

Dhenain, M., Michot, J.-L., Volk, A., Picq, J.-L., Boller, F., 1997. T2-weighted MRI studies of mouse lemurs: a primate model of brain aging. Neurobiol. Aging 18 (5), 517–521.

Dhenain, M., Michot, J.L., Privat, N., Picq, J.L., Boller, F., Duyckaerts, C., Volk, A., 2000. MRI description of cerebral atrophy in mouse lemur primates. Neurobiol. Aging 21 (1), 81–88.

Fernandez-Vizarra, P., Fernandez, A.P., Castro-Blanco, S., Serrano, J., Bentura, M.L., Martinez-Murillo, R., Martinez, A., Rodrigo, J., 2004. Intra- and extracellular Abeta and PHF in clinically evaluated cases of Alzheimer's disease. Histol. Histopathol. 19 (3), 823–844.

Good, C.D., Johnsrude, I.S., Ashburner, J., Henson, R.N., Friston, K.J., Frackowiak, R.S., 2001. A voxel-based morphometric study of ageing in 465 normal adult human brains. Neuroimage 14 (1 Pt 1), 21–36.

Gouras, G.K., Tsai, J., Naslund, J., Vincent, B., Edgar, M., Checler, F., Greenfield, J.P., Haroutunian, V., Buxbaum, J.D., Xu, H., Greengard, P., Relkin, N.R., 2000. Intraneuronal Abeta42 accumulation in human brain. Am. J. Pathol. 156 (1), 15–20.

Le Gros Clark, W.E., 1931. The brain of *Microcebus murinus*. Proc. Zool. Soc. Lond., 463–485.

Lee, V.M., Kenyon, T.K., Trojanowski, J.Q., 2005. Transgenic animal models of tauopathies. Biochim. Biophys. Acta 1739 (2–3), 251–259.

Mangin, J.-F., Coulon, O., Frouin, V., 1998. Robust brain segmentation using histogram scale-space analysis and mathematical morphology. Medical Image Computing and Computer-assisted Intervention—MICCAI'98, Springer-Verlag. Lect. Notes Comput. Sci. 1496, 1230–1241.

Mangin, J.F., 2000. Entropy minimization for automatic correction of intensity nonuniformity. In: IEEE Workshop, MMBIA, Hilton Head Island, South Carolina, pp. 162–169.

Oakley, H., Cole, S.L., Logan, S., Maus, E., Shao, P., Craft, J., Guillozet-Bongaarts, A., Ohno, M., Disterhoft, J., Van Eldik, L., Berry, R., Vassar, R., 2006. Intraneuronal beta-amyloid aggregates, neurodegeneration, and neuron loss in transgenic mice with five familial Alzheimer's disease mutations: potential factors in amyloid plaque formation. J. Neurosci. 26 (40), 10129–10140.

Oddo, S., Caccamo, A., Shepherd, J.D., Murphy, M.P., Golde, T.E., Kayed, R., Metherate, R., Mattson, M.P., Akbari, Y., LaFerla, F.M., 2003. Triple-transgenic model of Alzheimer's disease with plaques and tangles: intracellular Abeta and synaptic dysfunction. Neuron 39 (3), 409–421.

Perret, M., 1997. Change in photoperiodic cycle affects life span in a prosimian primate (*Microcebus murinus*). J. Biol. Rhythm. 12 (2), 136–145.

Tisserand, D.J., van Boxtel, M.P., Pruessner, J.C., Hofman, P., Evans, A.C., Jolles, J., 2004. A voxel-based morphometric study to determine individual differences in gray matter density associated with age and cognitive change over time. Cereb. Cortex 14 (9), 966–973.

Trouche, S.G., Asuni, A., Boutajangout, A., Frangione, B., Wisniewski, T., Rouland, S., Verdier, J.M., Sigurdsson, E.M., Mestre-Frances, N., 2008. Neuropathological evaluation of the nonhuman primate *Microcebus murinus* immunized with K6Abeta1-30, an Abeta derivative. Alzheimers Dement. 4 (4 Suppl. 2), T211.

Valk, J., Barkhof, F., Scheltens, P., 2002. Magnetic Resonance in Dementia. Springer-Verlag, Heidelberg/Berlin/New York, 353 pp.

Van Broeck, B., Vanhoutte, G., Pirici, D., Van Dam, D., Wils, H., Cuijt, I., Vennekens, K., Zabielski, M., Michalik, A., Theuns, J., De Deyn, P.P., Van der Linden, A., Van Broeckhoven, C., Kumar-Singh, S., 2008. Intraneuronal amyloid beta and reduced brain volume in a novel APP T714I mouse model for Alzheimer's disease. Neurobiol. Aging 29 (2), 241–252.

Wirths, O., Multhaup, G., Bayer, T.A., 2004. A modified beta-amyloid hypothesis: intraneuronal accumulation of the beta-amyloid peptide—the first step of a fatal cascade. J. Neurochem. 91 (3), 513–520.

Wirths, O., Multhaup, G., Czech, C., Blanchard, V., Moussaoui, S., Tremp, G., Pradier, L., Beyreuther, K., Bayer, T.A., 2001. Intraneuronal Abeta accumulation precedes plaque formation in beta-amyloid precursor protein and presenilin-1 double-transgenic mice. Neurosci. Lett. 306 (1–2), 116–120.